A Hydrogen Peroxide-Responsive O_2 Nanogenerator for Ultrasound and Magnetic-Resonance Dual Modality Imaging

*Fang Yang, Sunling Hu, Yu Zhang, Xiaowei Cai, Yan Huang, Feng Wang, Song Wen, Gaojun Teng, and Ning Gu**

The environmental stress from the exposure to toxin and drugs may induce the production of reactive oxygen species (ROS).[1] ROS are high-energy oxygen-bearing molecules encompassing a variety of chemical species including superoxide anions ($\bullet O_2^-$), hydroxyl radicals (•OH), hydrogen peroxide (H_2O_2), and so on.[2–4] ROS accumulated in living systems are often implicated as potent inducers of oxidative damage as well as mediators of ageing and inflammation.[5] The overproduction of ROS can damage cellular lipids, proteins, or DNA, thus inhibiting their normal function. ROS are also involved in numerous ailments ranging from cancer, diabetes mellitus, ischemia injury, and inflammatory diseases to neurodegenerative disorders.[6,7] Thus, it is important to detect and image ROS changes in complex biological microenvironments.

Being a representative ROS, H_2O_2 is freely diffusible and relatively long-lived,[8–10] which makes it a potential diagnostic marker for the presence and progression of a wide range of pathological states. In order to visualize H_2O_2 levels in vivo with high-sensitivity, up to now, numerous detection methods including fluorescent probes, electrochemical sensors and MR-imaging methods have been developed for the determination of H_2O_2.[11–15] However, conventional H_2O_2 probes have some limitations such as auto-oxidation, poor specificity, less sensitivity, and high cost for in vivo analysis.[16–19] With a surge of interest in combining modalities (ultrasound, computed tomography, magnetic-resonance imaging, optical imaging, etc), both as instruments and in probes,[20,21] the clinical utility for multimodal probes may be a new strategy for the detection of H_2O_2. Such techniques can actualize the complementary abilities of different clinical diagnostic imaging modalities and obtain more accurate information in living systems with good spatial and temporal resolution.

Ultrasound contrast agents (UCAs) have tremendous diagnostic potential because of their excellent contrast resolution and the widespread clinical uses. However, current UCAs are composed of pre-formed gas microbubbles, which are less stable after injection into the body.[22] Although some new "smart" contrast agents that only enhance the ultrasound (US) signal in a specific chemical environment have already been studied,[23,24] there are no UCAs that can image radical oxidants, especially for detection of H_2O_2 in a clinical setting. In order to understand the diverse roles of H_2O_2 in pathological conditions, we have developed a new strategy for performing in vitro and in vivo US and magnetic-resonance (MR) dual modality imaging of H_2O_2. It was demonstrated that Prussian Blue nanoparticles (PBNPs) ($KFe^{3+}[Fe^{2+}(CN)_6]$) possess catalase-like activity to catalyze breakdown of H_2O_2 into oxygen (O_2) molecules under the neutral pH condition (pH = 7.4). This chemical reaction that generates gas-bubble-forming molecules can be used as a UCA to enhance US imaging. In tissues that over-produce radical oxidants, PBNPs can react with radical oxidants to produce oxygen bubbles and therefore change the acoustic impedance of tissue experiencing oxidative stress to make it detectable by US imaging. Both an unusual structural feature that renders some of the Fe^{3+} centers accessible to water co-ordination and the paramagnetic oxygen bubbles can shorten the T_1 relaxation time, which is beneficial for offering a unique platform for developing nanoparticle-based T_1 MRI contrast agents. All of the results suggest that PBNPs are an attractive nanoparticle-based US as well as a T_1 MRI dual modal H_2O_2 responsive nanoplatform.

TEM images of samples after being air-dried onto a grid revealed a square morphology with an average diameter of about 50 nm (Supporting Information, Figure S1a). The mean hydrodynamic diameter of the poly(vinyl pyrrolidone) (PVP)-stabilized PBNPs was measured to be 126.7 ± 1.3 nm with a polydispersity index (PI) of 0.092 using the dynamic light scattering method. The UV–vis spectrum of the resulting PBNP solution showed a broad characteristic band with λ_{max} at 697.5 nm, which is consistent with an intermetal charge-transfer band from Fe^{2+} to Fe^{3+} in PBNPs (Figure S1b).[25,26]

Dr. F. Yang, S. Hu, Prof. Y. Zhang, X. Cai, Prof. N. Gu
State Key Laboratory of Bioeletronics
Jiangsu Key Laboratory for Biomaterials and Devices
School of Biological Science and Medical Engineering
Southeast University
Nanjing, 210096, China
E-mail: guning@seu.edu.cn
Y. Huang, Prof. F. Wang
Nuclear Medicine Department
Nanjing First Hospital
Nanjing Medical University
Nanjing, 210006, China
S. Wen, Prof. G. Teng
Department of Radiology
Zhong Da Hospital
School of Clinical Medicine
Southeast University
Nanjing, 210009, China

DOI: 10.1002/adma.201202367

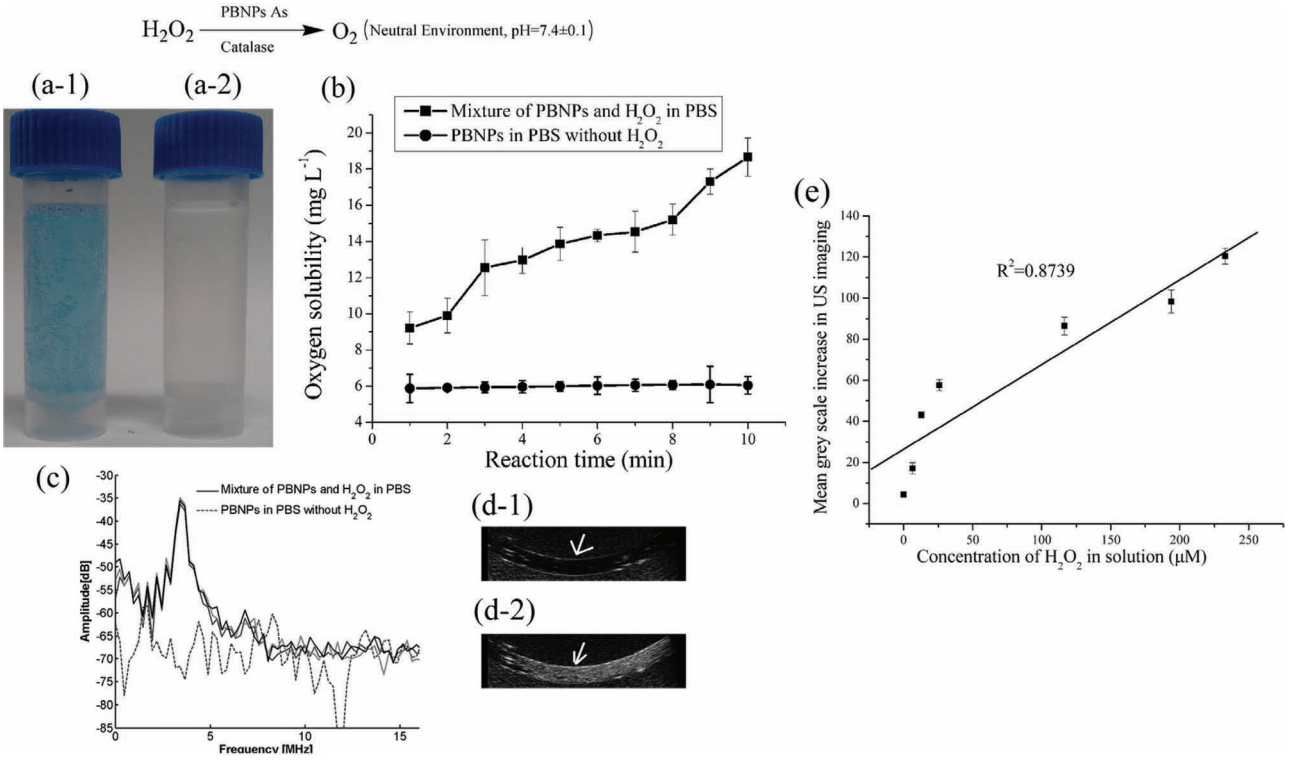

Figure 1. The generation of oxygen gas bubbles and acoustic response in vitro. a-1) The mixture of PBNPs and H_2O_2 solution in the PBS (pH = 7.4). a-2) The H_2O_2 solution in the PBS without the PBNPs. b) Oxygen-solubility change with the increase of reaction time. c) The generated gas bubbles in the PBS mixture of PBNPs and H_2O_2 display a great increase in acoustic signal intensity compared to the PBNPs in the PBS but without the H_2O_2. d-1) In vitro US imaging of the PBNPs in the PBS but without the H_2O_2. d-2) In vitro US imaging of the mixture of PBNPs and H_2O_2 in the PBS. e) The relationship between the mean grey scale of the US imaging enhancement and the concentration of H_2O_2. With the increase of the H_2O_2 concentration, the mean grey scale of the US images are also increased lineally in the range of 0–250 μM.

The concentration of the PBNPs was 2.26×10^{-9} M in terms of nanoparticle molar concentration.

When well-mixed solutions of PBNPs and the diluted H_2O_2 were added into phosphate buffer solution (PBS) (pH = 7.4) at room temperature (20 °C), plenty of bubbles were observed, as shown in **Figure 1**a–1. At the beginning of the reaction, the size of the bubbles was about 1 μm under observation by optical microscopy. When more and more bubbles emerged, the size could become bigger and bigger because of the growth of the bubbles or their aggregation. The final size of the generated bubbles may range from 5 μm to 30 μm. In contrast, when H_2O_2 solution was added into the PBS solution without PBNPs, there were no bubbles generated in the tube. It was found that under neutral conditions (pH = 7.4), PBNPs can catalyze the decomposition of H_2O_2 into O_2, which then dissolved into the solution and became free oxygen bubbles above the supersaturation limit of O_2. In order to prove further the existence of oxygen bubbles after reaction, the oxygen solubility was measured. The results are shown in Figure 1b. In PBS (pH = 7.4), the oxygen solubility in the mixture solution of H_2O_2 and PBNPs grows fast; but in the same conditions without PBNPs, the oxygen solubility did not change significantly and its curve tends to be flat. This phenomenon can directly confirm that PBNPs play a catalytic role of catalase-like in the decomposition of H_2O_2.

The sensitivity of US imaging to detect oxygen-gas formation from H_2O_2 decomposition is a key factor for reaction-based gas-bubble contrast agents. According to Fick's first law, in air-saturated water at 20 °C, the corresponding oxygen concentration is about 9 mg L^{-1}.[27] Our in vitro studies show that the oxygen solubility reached over 9 mg L^{-1} immediately after the 2.26 nM PBNPs mixed with 70 μM H_2O_2. Moreover, with the increase of the reaction time, the oxygen solubility grows almost exponentially (Figure 1b). The results show that the oxygen-gas generation is faster than gas diffusion for bubbles to nucleate. This is because the oxygen solubility could increase over the oxygen-gas supersaturation in the suspension immediately when mixing the PBNPs and H_2O_2, which ensures that gas-bubble nucleation can occur above the oxygen gas saturation concentration.

A custom-built in vitro US imaging and an acoustic measuring system were developed to prove quantitatively the ability of PBNPs in catalyzing the H_2O_2 to generate gas bubbles to be used as UCAs. Figure 1c demonstrates that strong acoustic echoes were obtained from free oxygen gas bubbles identified by the acoustic measuring system, which indicates that PBNPs can nucleate bubbles in the presence of H_2O_2 in the PBS (pH = 7.4) and can be detected acoustically. The perturbations induced by US as applied in process of chemical reaction could also enhance the bubble nucleation rate and

bubble growth via rectified diffusion and other mechanisms.[28] Figure 1d-1 shows an image of the cellulose tube only containing PBNPs in the PBS, which has no evidence of imaging enhancement. In contrast, after immediately injecting the mixture of PBNPs and H_2O_2 solution into the cellulose tube, the PBNPs became the gas-bubble nanogenerator to decompose H_2O_2 into O_2; then, the nucleated O_2 molecules can act as gas-bubble UCAs to enhance the US imaging and make the US images become brighter (Figure 1d-2). In order to understand what nanoparticle concentrations can produce a detectable response for a given H_2O_2 level, the same concentration of H_2O_2 solution (70 μM) was mixed with various concentrations of PBNPs (2.26×10^{-10} M, 4.52×10^{-10} M, and 2.26×10^{-9} M). The results show that the different concentrations of PBNPs can lead to different brightnesses of US images (58.6, 60.9, and 73.7 respectively). Although a bubble can be produced under a low concentration (2.26×10^{-10} M), the slower reaction rate may make it respond less sensitively to US imaging. Therefore, in the following experiments, the concentration of 2.26 nM was chosen.

Because the physiological concentration of free-radical oxidants is usually in the nanomolar to micromolar range,[29] we also investigated whether PBNPs could detect radical oxidants in this low concentration range. The same concentration of PBNPs solution (2.26 nM) was mixed with various concentrations of the H_2O_2 (0, 6, 12, 25, 116, 194, and 232 μM). Figure 1e shows the increase of the mean grey scale in US images under the same concentration of PBNPs solution (2.26 nM) well mixed with the above-mentioned various concentrations of H_2O_2. The results demonstrate that PBNPs can detect a hydroxyl radical concentration as low as 10 μM. It also displays a linear correlation between the ultrasound intensity and the hydroxyl radical concentrations within the range of 0–250 μM ($R^2 = 0.8739$). The different concentrations of H_2O_2 will lead to different mean grey-scale enhancement of the US images. According to the change of the mean grey scale of the US imaging enhancement, the existence of H_2O_2 can be determined accurately at real-time and with high resolution.

We further investigated the in vivo feasibility of using PBNPs to image oxidative stress in mice, induced by a lipopolysaccharide (LPS)-treated inflammatory response. **Figure 2**a illustrates that PBNPs can enhance acoustic contrast in mice liver experiencing oxidative stress while maintaining a low background signal in healthy mice. Ten minutes after the PBNPs injecting, several bright spots became visible in the livers of the LPS-treated mice, but not in the LPS-untreated mice injected with PBNPs (Figure 2c). It was also verified that injecting saline into the LPS-treated mice did not produce enhanced US echoes (Figure 2b), demonstrating that inflammation in tissues alone also did not enhance ultrasound echoes. In order to perform quantitative analysis on the US images when PBNPs were injected into the LPS-treated mice (n = 5), the typical mean grey-scale time-course of the US images in mice liver is shown in Figure 2d. The measurement of region of interests (ROIs) was selected from a relatively homogeneous four regions of the liver tissues according to the Figure 2a. After about 15 min of PBNPs injection, the normalized mean grey scale of US images in the liver of LPS-treated mice was increased by about 80%. However, the normalized mean grey scale of the US images remained at baseline intensity levels for LPS-untreated mice even injected with PBNPs. There was a significant difference between the groups with P values of 0.017 ($P < 0.05$). All of these results demonstrate that the PBNPs can detect oxidative stress in vivo with an excellent spatial resolution. The degree of relative oxidative stress can be predicated by the mean grey-scale

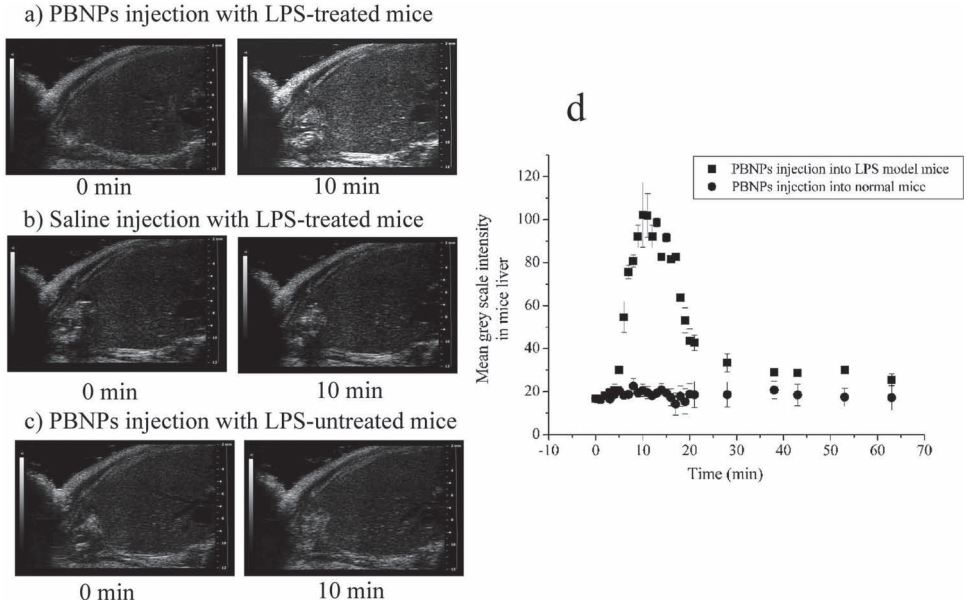

Figure 2. The PBNPs can enhance ultrasound contrast and image oxidative stress in vivo during LPS-induced inflammatory response. a) Representative US images of the mouse liver show enhanced US contrast 10 min after PBNPs injection. b,c) As a control experiment, saline was injected into the LPS-treated mice and PBNPs was injected into the normal mice, which shows that there are no significant imaging changes. d) Quantitative image analysis of the US-images enhancement demonstrates that PBNPs injected into the LPS-treated mice could significantly increase their normalized mean grey-scale intensity, compared to no increase for the LPS-untreated mice injected with the PBNPs. The vertical bars represent the standard error.

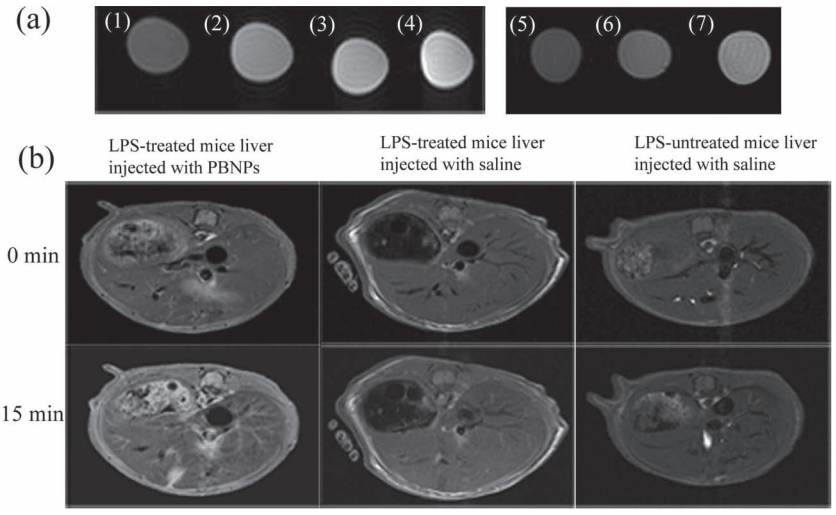

Figure 3. In vitro and in vivo MRI. a) PBNPs (2.26 nM) mixed with different concentrations of H_2O_2 ((1): 0 μM, (2): 5 μM, (3): 50 mM, (4): 250 mM) and H_2O_2 (50 mM) mixed with different concentrations of PBNPs ((5): 0 M, (6): 2.26×10^{-10} M, (7): 4.52×10^{-10} M) in PBS. b) Representative MRI images of the mouse liver show an enhanced MRI contrast 15 min after PBNPs injection into the LPS-treated mice, LPS-untreated mice injected with PBNPs, and saline.

intensity change of the US images, which offers a new and easy approach to understand quantitatively the H_2O_2 generation during the process of ROS-related pathological disease.

To investigate the potential use of PBNPs as an MRI contrast agent, we performed T_1 measurements in vitro and in vivo. **Figure 3**a shows MRI images of PBNPs in PBS solution, the mixtures of PBNPs (2.26 nM) with different H_2O_2 concentrations (5 μM, 50 mM, and 250 mM respectively) and H_2O_2 (50 mM) with different PBNP concentrations (0, 2.26×10^{-10} M, 4.52×10^{-10} M respectively). This comparison suggests that a greater production of O_2 results in a better contrast in the MRI image to change the T_1 signal. The longitudinal relaxivity value of PBNPs, r_1, is 0.0557 mM^{-1} s^{-1} and the transversal relaxivity value of PBNPs, r_2, is 9.47 mM^{-1} s^{-1}. As for the PBNPs themselves, the T_1 relaxivity seems a little low because of the biocompatible PVP modification on the PBNPs surface. However, under neutral conditions (pH = 7.4), PBNPs can catalyze H_2O_2 decomposition into oxygen. O_2 is paramagnetic; the dissolved molecular oxygen then shortens the T_1 relaxation time[30] and may be a major contributor to help in the MR T_1 imaging. Although use of such nanoparticles to enhance the T_2-weighted image contrast is also possible, a T_1 MRI contrast is generally preferred over T_2 MRI contrast due to the fact that darkened spots caused by artifacts such as bleeding or calcification may be mistaken for accumulation of the contrast agent. Therefore, PBNPs may provide a superior alternative to nanoparticle-based MRI T_1 contrast agent in our studies.

The T_1 MR images of the mice liver were recorded at scheduled temporal points pre- and post-injection of PBNPs. For mice treated with LPS and PBNPs, a significant increase of the signal intensity (SI) in the liver area was observed. Figure 3b shows the representative T_1 MRI images in vivo after 15 min injection of PBNPs. The results showed that the relative MRI SI in the region of liver was calculated to be 45 ± 4.8% higher than for pre-injection, but almost no signal change was found in LPS-untreated mice injected with saline. There was a significant difference between the groups with the P values of 0.025 ($P < 0.05$). The LPS-treated mice livers injected with saline had higher T_1 imaging enhancement than LPS-untreated mice livers injected with PBNPs, but had lower T_1 imaging enhancement than those treated with both LPS and PBNPs. Based on the MRI analyses, it is reasonable to conclude that the PBNPs can act as an effective T_1 MRI contrast agent to detect inflammation in liver tissues. This synthetic design paradigm, the co-operation between PBNPs itself and the generation of oxygen bubbles in the liver tissues, may represent a new generation of nanoparticle-based T_1 contrast agents for in vivo MR imaging. Another point worth mentioning is that, after recovering from anesthesia spontaneously, mice treated with PBNPs can live normally for weeks, demonstrating that PBNPs are not acutely toxic to the experimental animals. The in vitro RAW 264.7 cell cytotoxicity of PBNPs using the Trypan Blue exclusion method also indicates that no difference in cell viability was observed between untreated control cells and cells treated with PBNPs for 24 and 48 h (Figure S2) at concentrations comparable to the highest concentration used for the US and MR imaging studies.

To confirm further the existence of PBNPs in LPS- treated mice liver tissues, liver slices were resected at 2 h after injection of PBNPs in the normal and LPS-treated mice, then stained successively by nuclear fast red solution for the cell nuclei, and analyzed via optical microscopy. As shown in **Figure 4**, in the LPS-untreated mice and LPS-untreated mice but 2 h later with the injection of PBNPs, no histological alterations in the liver were observed (Figure 4a and 4b). Liver tissue specimens of LPS-treated mice with no PBNPs administration showed cytoplasmic vacuolation, focal nuclear pyknosis, and inflammatory cell infiltration (Figure 4c), which demonstrates that the LPS could trigger the inflammatory response in the mice liver. After PBNPs injection, each of these histopathological changes has markedly broadened as comparison of those seen in the LPS group with no PBNPs injection (Figure 4d). The widened intercellular space may be induced by the production of oxygen gas bubbles resulting from the reaction between the PBNPs and the H_2O_2 in the inflammatory liver tissue. The gas bubble in the liver tissue obliged more gaps in the liver tissue to emerge, which is consistent with the in vivo US and MR imaging analyses.

In summary, the overproduction of hydrogen peroxide (H_2O_2) induced by ROS can act as a potential diagnostic marker for the presence and progression of a wide range of pathological states. We report that Prussian Blue nanoparticles (PBNPs) possess a catalase-like activity to catalyze the breakdown of H_2O_2 into oxygen molecules under the neutral condition (pH = 7.4). Based on this finding, we have developed a new strategy in which PBNPs can be an excellent US and MR dual modality imaging probe for in vitro and in vivo diagnosing H_2O_2 with

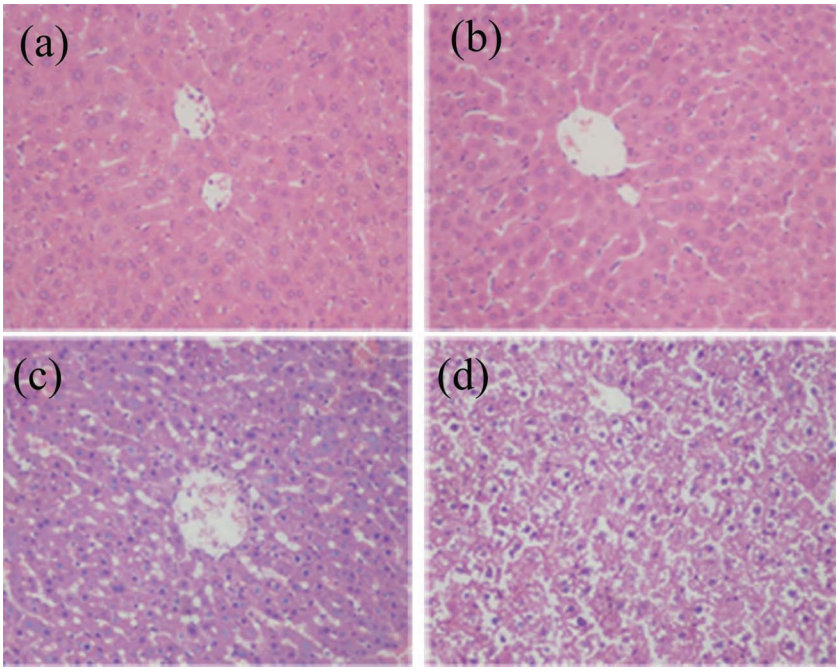

Figure 4. LPS-induced changes in mice liver histology. Ex vivo nuclear fast red double staining images of liver tissues excised from: a) untreated mice, b) untreated mice 2 h post-injection of PBNPs, c) LPS- treated mice, d) LPS- treated mice 2 h post-injection of PBNPs.

high sensitivity and resolution. Thus, PBNPs offer a versatile nanoplatform for potentially widespread clinical uses for investigation of H_2O_2 generation. This method may have great potential in unveiling the unknown physiological mechanisms related to H_2O_2.

Experimental Section

Materials: All of the chemicals used in this study were of analytical reagent grade and used as received. Ferric chloride ($FeCl_3{\bullet}6H_2O$), Ferrous chloride ($FeCl_2{\bullet}4H_2O$), dimethyl sulfoxide (DMSO), hydrochloric acid, potassium ferrocyanide ($K_4[Fe(CN)_6]{\bullet}3H_2O$), anhydrous sodium acetate, poly(vinyl pyrrolidone) (PVP), and acetic acid were all purchased from Sinopharm Chemical Reagent Co. Ltd. Hydrogen peroxide (H_2O_2, 30%) was from Aladdin Chemical Reagent Co. Ltd. Potassium ferricyanide ($K_3[Fe(CN)_6]$), tetramethylammonium hydroxide, sodium hydrogencarbonate, anhydrous sodium carbonate, sodium chloride, potassium chloride, and hydroxylammonium chloride were purchased from Shanghai Lingfeng Chemical Reagent Co. Ltd.

Preparation of PBNPs and Characterization: The PBNPs were prepared according to reported methods by using PVP as a protecting polymer.[25,26] In a typical synthesis, the concentration ratio of PVP to $[Fe^{2+}(CN)_6]^{4-}$ is 100 (Fe^{3+} = $[Fe^{2+}(CN)_6]^{4-}$ = 1 mM). Both $FeCl_3{\bullet}6H_2O$ (27 mg) and PVP (1,110 mg) were evenly dissolved in de-ioned and distilled water (80 mL). Then, the $K_4[Fe(CN)_6]$ solution (2 mg mL^{-1}, 20 mL) was added to the mixture solution by using micro-scale injection pump (WZS-50F6, Smiths Medical, USA) under stirring (1200 r min^{-1}) at a temperature of 60 °C to produce a clear, bright blue dispersion. The reaction mixture was then dialyzed by a 14 k molecular-weight cutoff (MWCO) dialysis bag under the condition of magnetic mixing to completely remove KCl, Fe^{2+}, $[Fe^{3+}(CN)_6]^{3-}$ or Fe^{3+}, and $[Fe^{2+}(CN)_6]^{4-}$. Lastly, the sample was filtered through a 220 nm aperture filter.

The particle size and morphology of the obtained PBNPs were characterized by dynamic light scattering (DLS) (ZetaPlus-Zeta Potential Analyzer, USA) and transmission electronic microscopy (TEM) (JEOL JEM-2100, Japan). UV–vis absorption spectra were measured using a UV–vis–NIR spectrophotometer (Shimadzu UV-3600, Japan) after 10 times dilution of the PBNPs samples.

The Chemically Generated Oxygen-Free Bubble with PBNPs In Vitro: In order to verify the generation of oxygen-free bubbles under neutral conditions (pH = 7.4), the catalase-like activity of PBNPs was determined at room temperature in two 15 mL centrifuge tubes, separately. One tube included PBNPs solution (0.30 mL, 2.26 nM, in terms of nanoparticle molar concentration), phosphate buffer saline (PBS) (9.00 mL, 0.01 M, pH = 7.4 ± 0.1), and H_2O_2 (0.07 mL, 1 M). A second tube was under the same conditions, just not adding the H_2O_2, but adding the same volume of water. Then, the dissolved oxygen electrodes, connected to a Multi-Parameter Analyzer (DZS-708, Cany Precision Instruments Co., Ltd), were put into the tubes to detect the oxygen solubility. With the increase of reaction time, both the oxygen solubilities in the two centrifuge tubes were measured and compared.

Acoustic Observation and US Imaging In Vitro: For further investigation of the possibility of PBNPs catalyzing H_2O_2 into O_2 and the oxygen molecules then nucleating to form gas bubbles for US imaging, we designed the following gas-bubble ultrasonic detection experiments. A custom-built ultrasound imaging and acoustic measuring system was developed, which could simultaneously visualize gas-bubble nucleation and characterize its acoustic properties. An ultrasound scattering spectroscopy method was used to measure the acoustic scattering spectrum of oxygen gas bubbles from the reaction in the PBS mixing with PBNPs and H_2O_2 solution. A broadband planar transducer (diameter 15 mm, centre frequency 3 MHz, –6 dB band 1.5–4.5 MHz, Panametrics, USA) was used as both the transmitter and receiver. An aluminium plate located at a distance of L = 10 cm was used to reflect the signal. A sound-permeable container with a thickness of d = 1.5 cm was inserted between the transducer and the reflective board, and was about 1 cm close to the latter. The samples injected into the container included a mixture of PBNPs and H_2O_2 in the PBS, the PBNPs in PBS without H_2O_2 respectively. A pulser/receiver (Panametrics 5900PR, USA) generated a broadband pulse signal and the pulse signal was set to be 1 μJ at a pulse repetition frequency of 1 kHz. The received signal was amplified by the pulser/receiver and recorded by a digital oscilloscope (Agilent 54810, USA) with a sampling frequency of 100 MHz s^{-1} and a sampling-point number of 2048. The measurements were carried out at room temperature. The sampled signal was transferred to an off-line computer for post-processing.

The US imaging experiment was performed using a digital B-Mode diagnostic ultrasonic scanner with a 3.5 MHz center frequency probe. A self-made plexiglass tank was filled with ultrasonic phantom, and there was a cellulose tube pipeline in the phantom for sample loading. At the bottom and wall of the tank container, there was a layer of sound-absorbing sponge to absorb the echo and avoid interference. The channels were located in the phantom with diameter of 9 mm, curving downward into an arc. The distance between the pipeline's deepest point and the upper interface of phantom was 40 mm. This layout was beneficial for fixing a sample solution to US imaging. The samples included the H_2O_2 in the PBS but without PBNPs, the mixture of H_2O_2 with different concentration of PBNPs in PBS, and the mixture of PBNPs with different concentrations of H_2O_2 in PBS. Each sample was pre-mixed homogeneously and immediately injected into the cellulose tube to acquire the US enhancing images under the same B–Mode US imaging.

US Imaging of Oxidative Stress with PBNPs In Vivo: All of the animal experiments were performed in compliance with guidelines set by the Animal Care Committee of the Southeast University. Two groups of CD-1 male mice (n = 5 per group), aged 8–10 weeks, were obtained from the center of Laboratory Animal Sciences of Nanjing Medical University (Nanjing, China). One group was inflammation-bearing mice. Another group was the control healthy mice. Inflammation was induced by injecting lipopolysaccharide (LPS) (≈15–20 μg kg^{-1}, Sigma–Aldrich, USA) in saline (1 mg mL^{-1}).[29] 20 h later, the mice were anaesthetized with isofluorane (1.5 vol-% at 2 L min^{-1}) and the fur on the chest and abdomen was removed. The control mice group was injected with saline in the same way. The mouse liver was imaged using a small animal ultrasound imaging system (VisualSonics Vevo 2100, Canada) after PBNPs (200 μL, 2.26 nM PBNPs per mouse) injection and obtaining the liver US imaging in real time. The imaging settings for the ultrasound system are center frequency of f = 30 MHz, MI = 0.05, gain = 1 dB. A grey-scale mapping function was used to calibrate the ultrasound video intensity to ensure the video-image results were in the linear region. The mean video intensity in the regions of interest (ROIs) of the liver was analyzed and normalized to the video intensity at the time of contrast agent injection (time = 0). As the control experiments, the same volume of saline solution was injected in the same way and the liver US images were obtained. The suspension was then injected through the tail vein of the mice.

In Vitro and In Vivo MRI experiments: An in vitro phantom study was performed using a 7.0 T Micro-MRI (PhamaScan, Bruker, Germany). The sample was placed in an Eppendorf tube of 1 cm in diameter. At the beginning of each measurement, automatic shimming and preparation scans were performed with the deionized water. The imaging parameters for T_1 fast spin-echo were set as repetition time (T_R) = 4000 ms, echo time (T_E) = 108 ms, number of excitations (N_{EX}) = 1, echo-train length = 16. Images were obtained with a matrix size of 256 × 256, a section thickness of 1 mm, and a field of view (FOV) of 30 mm × 30 mm. Then, we continuously measured the resulting change in the longitudinal relaxation time (T_1) of the sample suspension by recording the above-mentioned single-slice gradient-echo signal. No phase or frequency encoding was used. According to the monoexponential signal decay as a function of T_E, the T_1 of samples could be estimated. Then, the longitudinal-relaxivity values, r_1, were determined from the slope of the plot of $1/T_1$ as a function of sample concentration. The samples included PBS, PBNPs solution, and PBNPs well mixed with different concentrations of H_2O_2 (0, 5 μM, 50 mM, and 250 mM).

All of the animal MRI experiments were performed just the same as the in vivo US imaging. The in vivo MRI experiments were performed under the same experiment conditions with the use of a 3.8 cm circular surface coil in transmit/receive mode, conducted on a 7 T Micro-MRI (PharmaScan, Brukers, Germany). MR imaging of the mice was performed using a T_1 fast low-angle shot (FLASH) gradient echo sequence. The mice were anesthetized with isoflurane (1.5 vol-% at 2 L min^{-1}) via a nose cone. Body temperature was maintained at 37 °C. The suspensions were then injected through the tail vein of the mice. The parameters for T_1 images were T_R/T_E = 408 ms/3.5 ms, flip angle = 30°, FOV = 35 mm × 35 mm, slice thickness = 1 mm, matrix = 256 × 256. The signal intensity (SI) was measured in the liver area; ROIs in the liver were also measured. The relative signal increase (RSD) (%) was calculated by using SI measurements before (SI pre) and after (SI post) each time point of PBNPs injection according to the following formula: $RSD\% = 100\ [(SI_{post\ in\ liver}) - (SI_{pre\ in\ liver})]/(SI_{pre\ in\ liver})$. The total imaging observation time was 2 h for each mouse.

Cell-Viability Assay: RAW 264.7 cells were cultured in RPM 1640 media containing 10% fetal bovine serum (FBS) at 37 °C and 5% CO_2. Cells were seeded in a 12-well plate at 75 000 cells per well. The cells were then incubated for 24 and 48 h with PBNPs (80 μg/ml calculated in forms of Fe element). The cells were then trypsinized and re-suspended in RPM 1640 media (250 mL), which was then added to a 0.4% Trypan Blue solution (250 mL). Viable and non-viable cells were counted using a hemocytometer. The results are expressed as the percentage of viable cells. All of the samples were run at least in triplicate.

Liver Histology Study: The inflammation-bearing mice and the LPS-untreated mice were sacrificed 2 h after PBNPs administration under pentobarbitone anesthesia; the livers were quickly removed and were fixed in 10% formalin, embedded in paraffin, and cut into 4 mm thick sections, stained successively by nuclear fast red for cell nucleus, and examined by optical microscopy. The inflammation-bearing and the LPS-untreated liver tissues from the control mice injected with saline were also dissected and treated using the same procedures as the control experiment.

Statistical Evaluation: The data are expressed as mean ± standard error (SE) with a sample size of 3 for in vitro ultrasound characterization. For in vivo studies, the data were expressed as means ± SE with a sample number of 5. The data were evaluated statistically using SPSS 13.0 Software (Chicago, USA). Comparisons were conducted using one-way analysis of variance (ANOVA) followed by a Student's t test. A value of $p < 0.05$ was considered statistically significant.

Supporting Information

Supporting Information is available from the Wiley Online Library or from the author.

Acknowledgements

This investigation was financially funded by the National Key Basic Research Program of China (Nos. 2011CB933503), National Natural Science Foundation of China (Nos. 31000453, 60725101, 31170959), Natural Science Foundation of Jiangsu Province (Nos. BK2011036, BK2009013). Funding also partially comes from the China-US International Science and Technology Co-operation Program (Grant No. 2009DFA31990).

Received: June 12, 2012
Published online: July 18, 2012

[1] R. Medzhitov, *Nature* **2008**, *454*, 428.
[2] M. Valko, D. Leibfritz, J. Moncol, M. T. D. Cronin, M. Mazura, J. Telser, *Int. J. Biochem. Cell B.* **2007**, *39*, 44.
[3] M. Schäferling, D. B. M. Grögel, S. Schreml, *Microchim. Acta* **2011**,*174*, 1.
[4] M. Giorgio, M. Trinei, E. P. Migliaccio, G. Pelicci, *Nat. Rev. Mol. Cell Biol.* **2007**, *8*, 722.
[5] X. Chen, X. Tian, I. Shin, J. Yoon, *Chem. Soc. Rev.* **2011**, *40*, 4783.
[6] T. Finkel, N. J. Holbrook, *Nature* **2000**, *408*, 239.
[7] Y. R. Kou, K. Kwong, L.Y. Lee, *J. Am. Chem. Soc.* **2011**, *133*, 3776.
[8] S. G. Rhee, *Science* **2006**, *312*, 1882.
[9] K. Zhang, R. J. Kaufman, *Nature* **2008**, *454*, 455.
[10] S. G. Rhee, T. S. Chang, W. Jeong, D. Kang, *Mol. Cell* **2010**, *29*, 539.
[11] Y. Zhang, H. Q. Luo, N. B. Li, *Biosyst. Eng.* **2011**, *34*, 215.
[12] W. Chen, Q. Q. Ren, Q. Yang, W. Wen, Y. D. Zhao, *Anal. Lett.* **2012**, *45*, 156.
[13] C. K. Lim, Y. D. Lee, J. Na, J. M. Oh, S. Her, K. Kim, K. Choi, S. Kim, I. C. Kwon, *Adv. Funct. Mater.* **2010**, *20*, 2644.
[14] E. W. Miller, O. Tulyathan, E. Y. Isacoff, C. J. Chang, *Nat. Chem. Biol.* **2007**, *3*, 263.
[15] M. C. Y. Chang, A. Pralle, E. Y. Issacoff, C. J. Chang, *J. Am. Chem. Soc.* **2004**, *126*, 15392.
[16] B. C. Dickinson, C. J. Chang, *J. Am. Chem. Soc.* **2008**, *130*, 9638.
[17] H. Koo, M. S. Huh, J. H. Ryu, D. E. Lee, I. C. Sun, K. Choi, K. Kim, I. C. Kwon, *Nano Today* **2011**, *6*, 204.

[18] E. K. Lim, Y. M. Huh, J. Yang, K. Lee, J. S. Suh, S. Haam, *Adv. Mater.* **2011**, *23*, 2436.
[19] A. R. Lippert, K. R. Keshari, J. Kurhanewicz, C. J. Chang, *J. Am. Chem. Soc.* **2011**, *133*, 3776.
[20] A. Louie, *Chem. Rev.* **2010**, *110*, 3146.
[21] F. M. Kievit, M. Zhang, *Adv. Mater.* **2011**, *23*, H217.
[22] F. Kiessling, S. Fokong, P. Koczera, W. Lederle, T. Lammers, *J. Nucl. Med.* **2012**, *53*, 345.
[23] B. P. Timko, T. Dvir, D. S. Kohane, *Adv. Mater.* **2010**, *22*, 4925.
[24] M. A. Nakatsuka, M. J. Hsu, S. C. Esener, J. N. Cha, A. P. Goodwin, *Adv. Mater.* **2011**, *23*, 4908.
[25] M. Shokouhimehr, E. S. Soehnlen, J. Hao, M. Griswold, C. Flask, X. Fan, J. P. Basilion, S. Basu, S. D. Huang, *J. Mater. Chem.* **2010**, *20*, 5251.
[26] T. Uemura, S. Kitagawa, *J. Am. Chem. Soc.* **2003**, *125*, 7814.
[27] C. Pénicaud, S. Peyron, N. Gontard, V. Guillard, *Food Rev. Int.* **2012**, *28*, 113.
[28] J. Wu, W. L. Nyborg, *Adv. Drug Delivery Rev.* **2008**, *60*, 1103.
[29] S. Hagiwara, H. Iwasaka, A. Hasegawa, S. Hidaka, A. Uno, K. Ueo, T. Uchida, T. Noguchi, *J. Surgical Res.* **2011**, *171*, 777.
[30] Y. Ohno, H. Hatabu, *Eur. J. Radiology* **2007**, *64*, 320.